Unusually thickened crust beneath the Emeishan large igneous province detected by virtual deep seismic sounding

Zhen Liu[a], Xiaobo Tian[a,b,*], Yun Chen[a], Tao Xu[a,b], Zhiming Bai[a], Xiaofeng Liang[a], Javed Iqbal[c], Yigang Xu[d]

[a] State Key Laboratory of Lithospheric Evolution, Institute of Geology and Geophysics, Chinese Academy of Sciences, Beijing 100029, China
[b] CAS Center for Excellence in Tibetan Plateau Earth Sciences, Beijing 100101, China
[c] Department of Earth Sciences, Abbottabad University of Science and Technology, Abbottabad, Pakistan
[d] State Key Laboratory of Isotope Geochemistry, Guangzhou Institute of Geochemistry, Chinese Academy of Sciences, Guangzhou 510640, China

ARTICLE INFO

ABSTRACT

The Emeishan Large Igneous Province (ELIP) in southwest China represents the erosional remnant of a vast basalt field emplaced during the Permian Period. Spanning 0.25 million km^2, the ELIP occupies a relatively small area relative to other Large Igneous Provinces (LIPs) such as the Siberian Traps and Ontong Java Plateau. The original volume of an ancient LIP can be constrained from estimates of its intrusive component. We used virtual deep seismic sounding (VDSS) to detect the boundary between the crust and the upper mantle (Moho) beneath the ELIP. A strong set of reflections from depths of 60–70 km indicate an unusually thick crust having a *P*-wave velocity of 7.0–7.4 km/s located beneath the inner zone of the ELIP. A high-velocity lower crustal body (HVLCB) of this thickness may have been formed by ponding magmas derived from the Emeishan mantle plume and associated fractionated materials. Combined images of crustal structure allow re-estimation of Emeishan magmatic volume. With a total estimated volume of 1.76–3.2×10^6 km^3, the ELIP appears to have been a typical sized plume-generated LIP relative to other global examples.

1. Introduction

Current geochemical models hold that Large Igneous Provinces (LIPs) can significantly alter the hydrosphere and atmosphere through their mass, heat, chemical and particulate fluxes within discrete periods of geologic time. The interpretation that LIPs can perturb climate is based on their large dimensions, high crustal production rates, and their temporal overlap with other evidence of major environmental change (Larson, 1991; Coffin and Eldholm, 1994). With vast areal coverage of at least 0.1 million km^2 (Coffin and Eldholm, 2001), LIPs are the most significant accumulations of mafic material on the Earth's surface after mid-ocean ridge basalts. While exact mechanisms for generating LIPs are still a matter of debate, the leading models include passive decompression melting beneath rifting continental lithosphere (e.g., White and Mckenzie, 1989), edge-driven convection (e.g., King and Anderson, 1998), mantle upwelling resulting from meteorite impact (e.g., Rogers, 1982), and most commonly, mantle plume activity (e.g., Morgan, 1971). The dimensions of mafic emplacement have been used to estimate the thermal anomalies and origination depth for individual LIPs (Furlong and Fountain, 1986).

In comparing major LIP categories: oceanic plateaus, continental flood basalts, volcanic passive margins, submarine ridges, seamount groups, and ocean basin flood basalts, Coffin and Eldholm (1994) found that major LIP types share several common features and differ significantly from normal oceanic or continental crust. LIPs specifically consist of an extrusive upper crust and a lower crust that exhibits high *P*-wave velocities (7.0–7.6 km/s). Mantle plume-derived melts pond in the lower crust or in upper zones of the upper mantle where they fractionate and form high-velocity lower crustal bodies (HVLCBs). As magma reservoirs in the deep crust, HVLCBs may contain large amounts of fractionated olivine and pyroxene along with minor amounts of plagioclase. HVLCBs therefore represent subsurface volumes on the same order of magnitude (at least) as that of erupted basalts (Farnetani et al., 1996). The intrusive/extrusive ratios vary from 1:1 to as much as 10:1, thus demonstrating the considerable volumetric range of LIP source material (White et al., 2006). Estimates for HVLCBs can elucidate the interaction between plume heads and the crust during LIP formation. As such they can also help constrain total LIP emplacement volume.

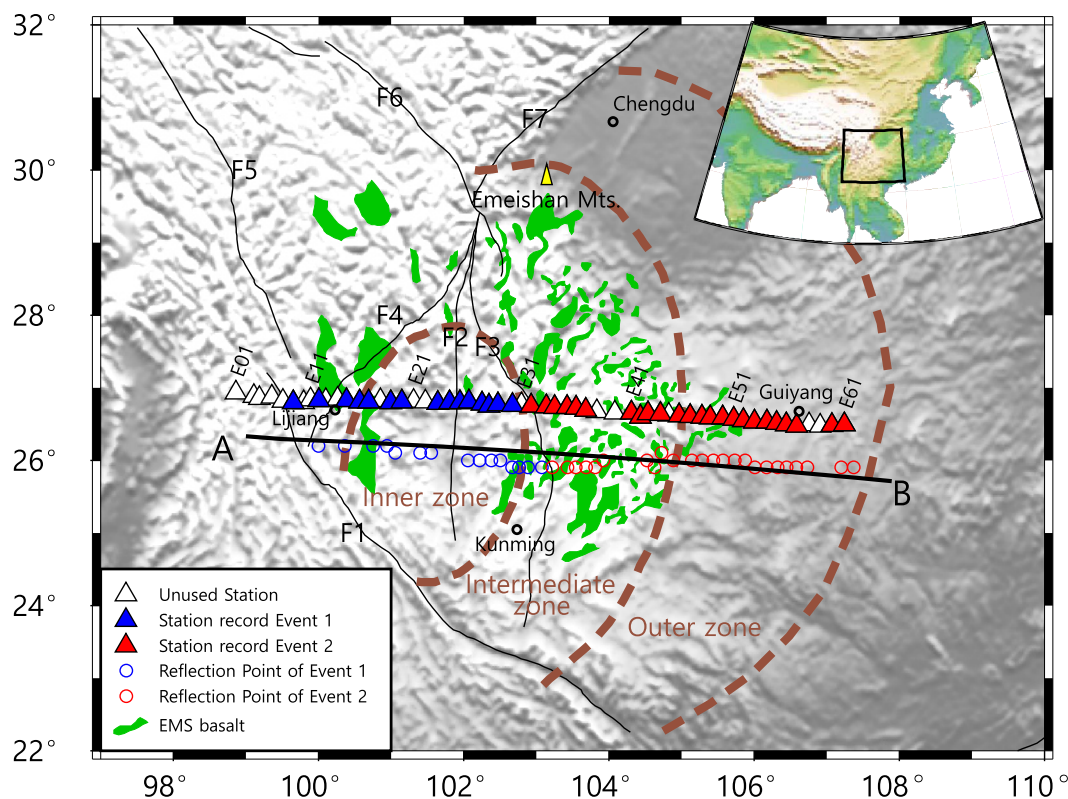Dobretsov et al. (2008) proposed that the Emeishan, Tarim and

---

Fig. 1. Shaded-relief map showing the geological features of the ELIP. The background of the map represents topographic relief. Triangles indicate the location of the COMPASS-ELIP seismic array. Blue triangles are stations aligned along the west branch, which record event 1 (Table 1). Red triangles are stations deployed along the east branch and record event 2 (Table 1). White triangles are stations not used in this study. Circles mark the locations of signal reflection points. The black solid line AB indicates the approximate location of the VDSS profile. The brown dashed lines indicate the inner, middle and outer zones in ELIP. The spatial distribution of Permian basalts (green areas) from Xu et al. (2004) and Xu and He (2007). Abbreviations for faults: F1, Red River Fault (RRF); F2, Lvzhijiang-Yuanmou Fault (LYF); F3, Xiaojiang Fault (XJF); F4, Lijiang-Xiaojinhe Fault (LXF); F5, Jinshajiang Fault; F6, Xianshuihe Fault (XSF); F7, Longmenshan Fault (LMF). The inset in the top right corner shows the study area bounded by a sector on a wider map. (For interpretation of the references to color in this figure legend, the reader is referred to the web version of this article.)

Siberian LIPs represent discrete plume pulses from a common source that originated near the core-mantle boundary. Xu et al. (2004) similarly interpreted the late Permian Emeishan large igneous province (ELIP) in southwest China (Fig. 1) as generated by a mantle plume. The ELIP's surface exposure of around 0.25 million km² is relatively small compared with typical LIPs such as the Siberian Traps and Ontong Java Plateau. Erosion and tectonic dismembering may have helped curtail the apparent size of the province. The overall ELIP complex divides into inner, intermediate, and outer zones based on the degree to which the underlying Maokou limestone is eroded out from beneath the basalt (He et al., 2003). Systematic spatial variation in the distribution and thickness of clastic and carbonate sediments across a pre-volcanic kilometer-scale lithospheric dome as well as the extent of erosion, thickness, and the chemistry of volcanic rock all indicate that the ELIP formed from a mantle plume (He et al., 2003; Xu et al., 2004).

The original volume of an ancient LIP can be constrained from the volume of its intrusive bodies. While consensus holds that the ELIP represents thickened crust (Xu and He, 2007), deep seismic sounding (DSS) studies have not consistently detected a HVLCB beneath the ELIP (e.g., Cui et al., 1987; Zhang et al., 1988; Xu et al., 2015). Other aspects of crustal structure beneath this region remain a matter of debate as well. Various seismic studies (Xiong et al., 1993; Li et al., 2006; Chen et al., 2010; Sun et al., 2012) have yielded inconsistent estimates of crustal thickness. These studies have used different data and methods including deep seismic sounding and *P*-wave receiver function analysis. Resulting estimates at different resolutions give uncertainties of greater than 10 km for both inner and outer zones of the ELIP. This large an uncertainty in crustal thickness estimates precludes accurate estimation the original ELIP volume and verification of the mantle plume model.

The uncertainty specifically prevents definitive observation of the gradual decrease in crustal thickness from the center to the edge of the dome, a feature diagnostic of the mantle plume mechanism (Xu et al., 2004).

A comprehensive geophysical investigation was conducted across the ELIP in order to characterize the subsurface structure and determine how it formed. This investigation used data provided by COMPASS-ELIP, a temporary broadband seismometer profile, COMWIDE-ELIP, a deep seismic sounding profile, and COMGRA-ELIP, a gravity investigation profile. Receiver function results from COMPASS-ELIP show that the Moho lies flat at depths of ~50 km beneath the inner zone and rises to depths of ~40 km in the outer zone (Chen et al., 2015). The amplitude of the *Pms* phase converted at the Moho depends on differences in wave-impedance above and below the Moho and can thus be obscured by any other strong discontinuities near the Moho. The crustal structure image provided by COMWIDE-ELIP indicates that the Moho lies at slightly shallower depths than those estimated by receiver function analysis (COMPASS-ELIP) (Chen et al., 2015; Xu et al., 2015). This discrepancy may be due to the fact that the active sources did not have sufficient energy to detect deeper structures. The COMGRA-ELIP gravity anomalies present the inner zone as a positive anomaly (Deng et al., 2014a, 2014b) and detect a high-density lower crustal body in the inner zone (Deng et al., 2016). This assumes a flat input model (Deng et al., 2016) as suggested by previous seismic evidence (Chen et al., 2015; Xu et al., 2015). However, such a result may not satisfy isostatic constraints as well as assuming higher-density lower crust in the inner zone for the given crustal thickness and mantle density. Isostatic balance requires either a thinner crust in the inner zone to reduce the mass of the crust or a thicker crust in the inner zone to provide the buoyancy
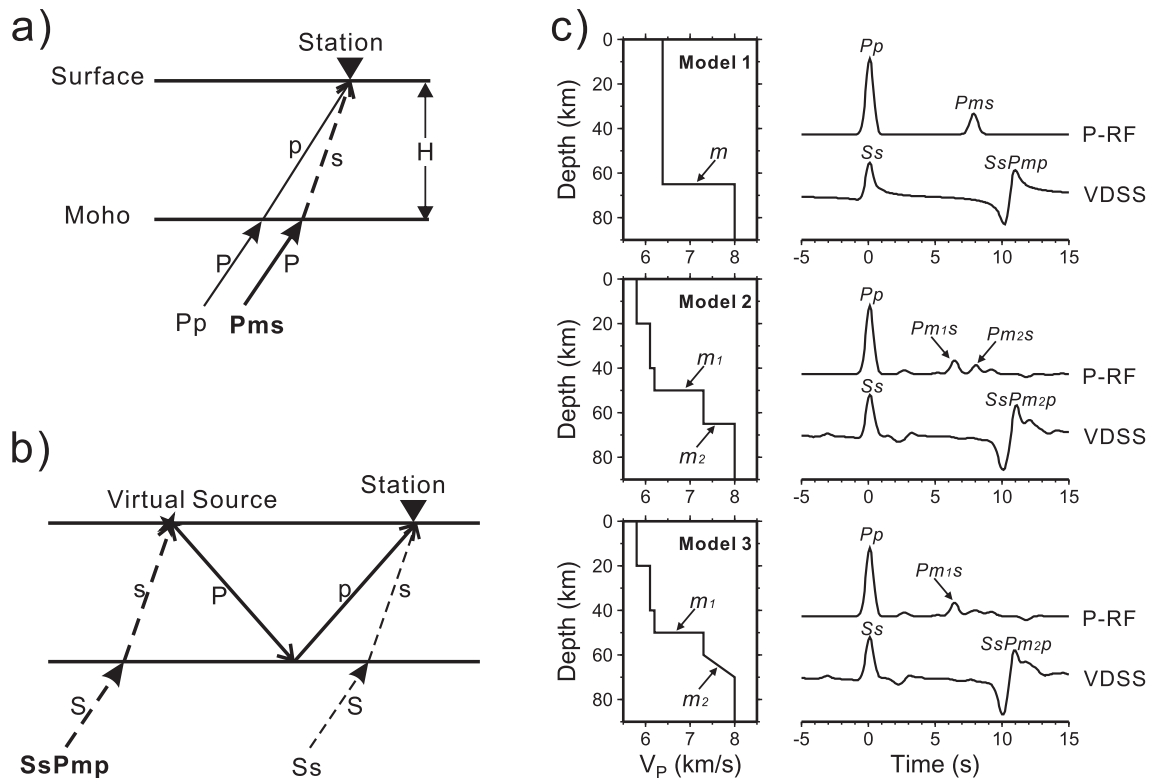
Fig. 2. Schematic diagrams illustrating the ray-paths of non-converted and converted seismic phases: (a) *Pp* and *Pms* (converted phase at the Moho); (b) *Ss* and *SsPmp* (converted phase and reflected at the Moho). In this last case, the signal can be considered an *S*-wave generated by a virtual source at the surface, which is reflected at the Moho (*Pp*- or *Pmp*-wave) and then arrives at the station. (c) The left column shows three velocity-depth models used to synthesize theoretical seismograms. The letters m, m1 and m2 mark distinct velocity discontinuities that might be interpreted as the crust-mantle boundary, i.e. the Moho. The rightmost column shows the synthetic waveforms of *P*-wave receiver functions (P-RF) and the waveforms obtained by virtual deep seismic sounding (VDSS) method from the respective velocity models on the left. In addition to the direct *Pp* and *Ss* waves, the *Pms* and *SsPmp* converted seismic phases are also indicated on the P-RF and VDSS waveforms.

necessary for supporting the heavier crust.

This research estimates crustal thickness using Virtual Deep Seismic Sounding (VDSS) methods (Tseng et al., 2009; Yu et al., 2013; Tian et al., 2015) with teleseismic data recorded by the COMPASS-ELIP experiment. Results are compared with receiver function (Chen et al., 2015) and DSS (Xu et al., 2015) results to confirm lower crustal structure.

2. Methods and data

This study used the VDSS method developed by Tseng et al. (2009) to investigate the structure of the crust and uppermost mantle beneath the ELIP. Unlike conventional DSS profiles with active, near-surface sources, VDSS utilizes the *S*- to *P*-wave conversion of teleseismic signals at the free surface (near the receiver) as a virtual seismic source (Fig. 2). The *SsPmp* seismic phase originates from the reflection of the direct *S*-wave at the free surface. This interaction partially converts the *S*-wave to a *P*-wave, which in turn, reflects off the Moho before travelling to a seismic station (Fig. 2b). The VDSS method produces large, clear reflections, which are insensitive to details of the Moho transition and thus provide a robust estimate of overall crustal thickness. For the simple case of a uniform crustal layer over a half-space mantle, the differential time between *SsPmp* and *Ss* arrivals ($T_{SsPmp - Ss}$) is

$$T_{SsPmp-Ss} = 2H (1/V_P^2 - p^2)^{\frac{1}{2}}$$

where p is the ray-parameter (horizontal slowness) of the incoming *S*-wave, H is the crustal thickness, and V_P is the *P*-wave velocity in the crust.

Fig. 2 demonstrates that in the *P*-wave receiver function method, Moho depth is detected by Moho conversion of the *Pms* phase whose

amplitude depends on the difference in wave-impedance above and below the Moho. The VDSS method estimates crustal thickness using the *SsPmp* phase, a waveform entirely reflected from upper mantle, which has a high *P*-wave velocity. Synthetic waveform modeling (Fig. 2c) shows that a high *P*-wave velocity (V_P) lower crust or wide Moho transition zone can weaken or even eliminate the *Pms* signal. The VDSS method, by contrast, produces clear, high-amplitude *SsPmp* reflections from the Moho. These are less sensitive to fine details but provide a more robust estimate of overall crustal thickness.

We used data from the COMPASS-ELIP experiment conducted at 27°N latitude between Fugong in western Yunnan and Guiding in central Guizhou (Chen et al., 2015). The profile consists of 59 seismographs deployed at station intervals of ~15 km for a total length of ~850 km. The profile was divided into two segments according to observation period. The West-Line (E01–E31) was deployed from November 2010 to November 2011 and the East-Line (E32–E61) was deployed from December 2011 to April 2013 (Chen et al., 2015). During these two periods, the array recorded more than 5000 earthquakes of magnitude 5.0 or larger.

We selected large to moderate-sized events between epicentral distances of 30° to 50° to enhance amplitudes of relevant seismic phases and minimize the influence of triplicate travel time. Two earthquakes were subject to detailed analysis (Table 1). We isolated vertical and radial components of the *S*-wave within a −10 s to 35 s window of its arrival. A zero-phase Butterworth band-pass filter (~0.05–0.5 Hz) was applied to enhance the signal-to-noise ratio. To enhance both the quality and quantity of VDSS results, we followed the approach of Yu et al. (2013) for removing effects of the earthquake source wavelet and near-source scattering through particle motion analysis and deconvolution of the vertical component from the pseudo-*S* wave. After deconvolution, the vertical component amplitude of the *SsPmp* phase was

Table 1
Reference earthquakes used in the VDSS method.

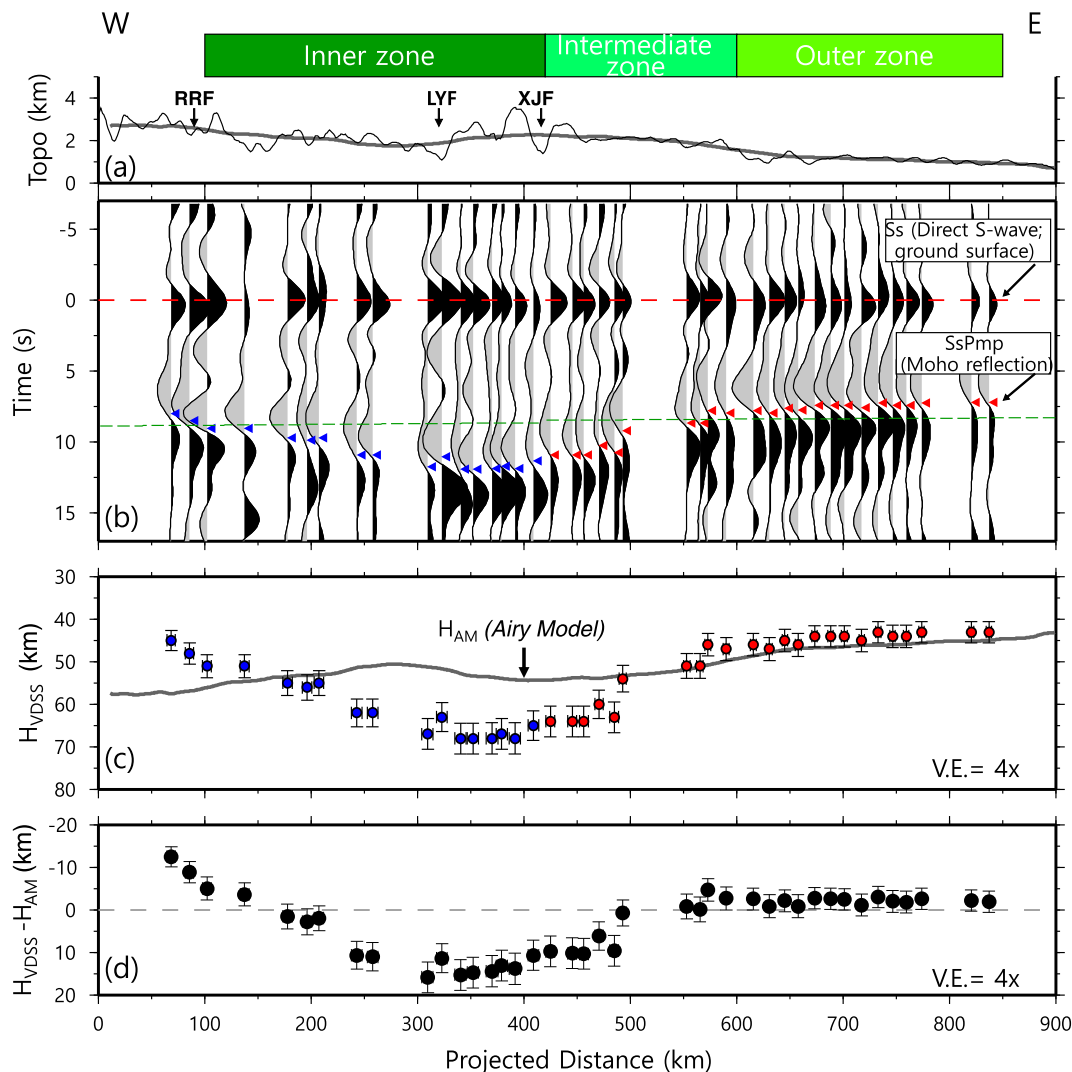| Event no.	Date	Origin time (UT)	Lat. (°N)	Lon. (°E)	Depth (km)	Mag.	Back-azimuth (°)	Distance (°)	Ray-parameter (*Ss* phase) (s/km)
1	2011/03/10	17:08:36	− 6.87	116.7	510	6.6 Mw	151–156	36.3–37.7	0.1330–0.1341
2	2012/09/03	18:23:05	− 10.7	113.9	14	6.2 Mw	162–169	37.8–38.9	0.1353–0.1362

Fig. 3. (a) ELIP. The location of the main faults covered by the profile (F1, F2 and F3 in Fig. 1) are identified by their respective abbreviations and marked by small arrows (RRF, Red River Fault; LYF, Lvzhijiang-Yuanmou Fault; XJF, Xiaojiang Fault). The continuous line running from west to east indicates average terrain elevation. (b) Reflected *P*-wave arrivals obtained from the *SsPmp* phases combined from the two earthquakes (Table 1). The red dashed lines indicates the arrival time of direct *S*-wave, while the arrow markers indicate the arrival time of the *SsPmp* phases (the blue and red arrows are for events 1 and 2, respectively, see Table 1). The *SsPmp* phase experiences a shift of ~π/2 with respect to the direct *S*-wave as a result of the total reflection at the top of Moho. The arrival time corresponding to the crustal thickness of 50 km for the whole profile is marked as a green dashed line. (c) Estimated crustal thickness (blue and red dots) based on times *TSsPmp-Ss* and average crustal *P*-wave velocity. The crustal thickness predicted by an Airy isostatic compensation model is indicated by a solid curve. (d) Difference between the crustal thickness estimated by VDSS and the thickness predicted from Airy isostasy. Vertical exaggeration in (c) and (d) is 4:1. (For interpretation of the references to color in this figure legend, the reader is referred to the web version of this article.)

sufficiently large to produce a clear signal. Fig. 3 shows seismograms aligned by their direct *S*-wave pulses. Robust signals from the Moho (the *SsPmp* phase) are observed from the two reference events. Note that there is a phase shift of 90 ± 30° between *Ss* and *SsPmp* phases because the latter experiences total reflection off the Moho at epicentral distances of 30° to 50°.

To determine the $T_{SsPmp-Ss}$, we compared the observed and synthetic seismograms calculated using the reflectivity algorithm (Randall, 1989) (Fig. 4). Tseng et al. (2009) and Yu et al. (2013) provide a detailed description of this methodology, which is an excellent tool for imaging the Moho under conditions of greatly thickened crust. The

SsPmp arrival time from ~7.2 s to ~11.9 s is marked by a triangle in each seismogram (Fig. 3b). The upper estimates for $T_{SsPmp-Ss}$ of 10.7 s to 11.9 s correspond to crustal thicknesses of about 60–70 km at a projected distance of 200 km and 500 km respectively along the profile AB.

The *P*-wave travel-time tomography image showed that V_P varies by less than ± 2% over a distance of 650 km along the DSS profile (COMWIDE-ELIP experiment, located along the passive seismic array between stations E13 and E57) spanning the ELIP (Chen et al., 2015; Xu et al., 2015). Even though T_{SsPmp} depends on both H and V_P, velocity perturbations in the tomographic model result in changes of only
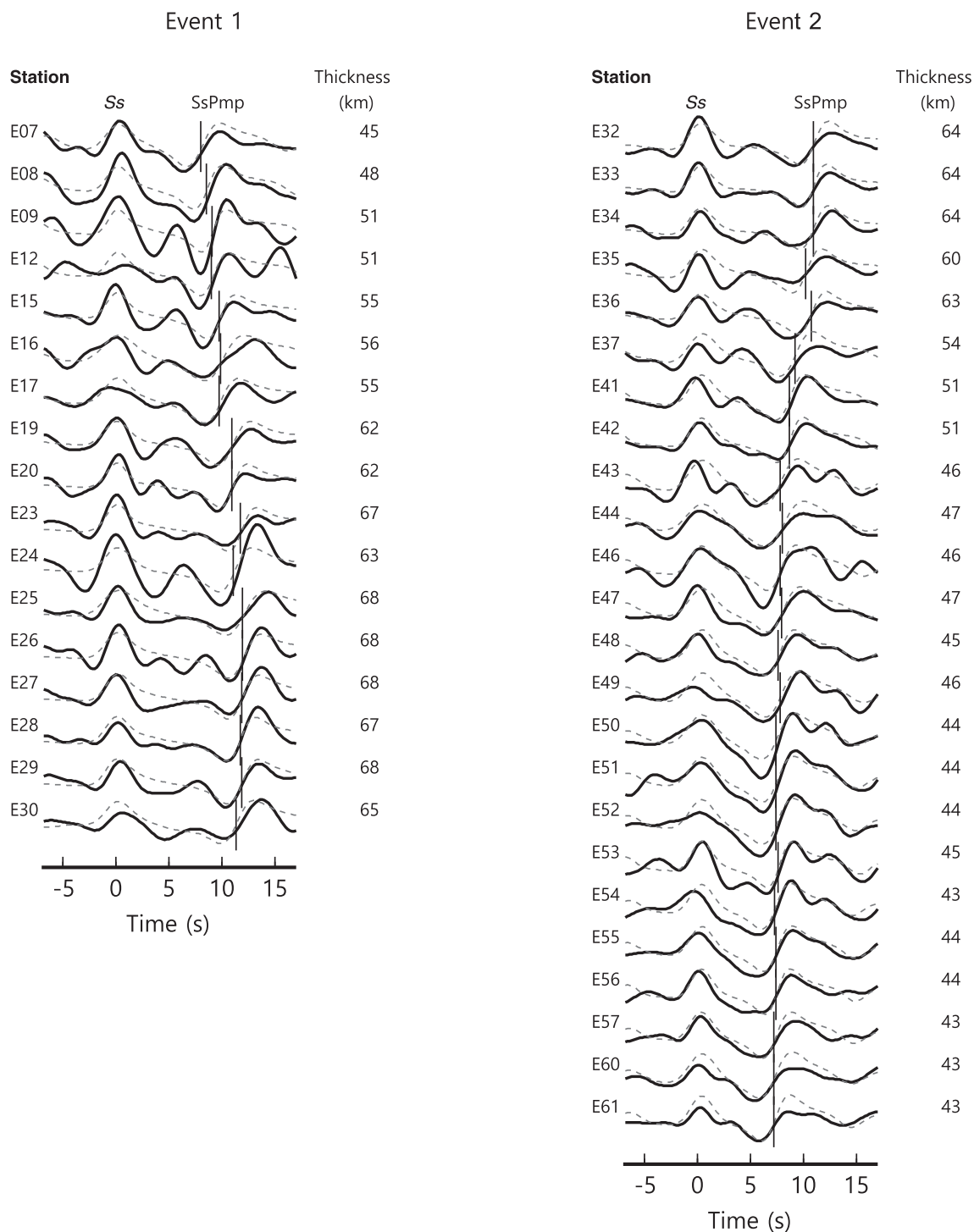
Fig. 4. Comparison of observed waveforms (solid lines) and the best-fit synthetic waveforms (dash lines) at the stations indicated in relation to the two test earthquakes considered in this study (events 1 and 2 in Table 1). The vertical bars mark the arrival time of the (converted and reflected) *SsPmp* phase, which is delayed with respect to the direct *Ss* wave. Estimated crustal thicknesses are given behind the waveforms.

about ± 4 km in estimated crustal thickness. A tightly constrained V_P value is not necessary for detecting first-order, relative changes in crustal thickness among different stations (Tseng et al., 2009). To estimate the crustal thickness (*H*) along the VDSS profile in Fig. 3b, we modeled the *SsPmp* based on a simple 1-D model with an average crustal V_P. The average V_P across the entire profile was assumed to be 6.3 km/s, consistent with estimates from the CRUST 1.0 model (http://igppweb.ucsd.edu/~gabi/rem.html). The observed variations in $T_{SsPmp - Ss}$ shown in Fig. 3b therefore largely reflect changes in average

crustal thickness. We nevertheless included a ± 0.1 km/s uncertainty in V_P when calculating crustal thickness (error-bars in Fig. 3c).

3. Results

Fig. 4 compares observed and best-fit synthetic waveforms. Since the phase and amplitude of post-critical *SsPmp* change with *P*-wave speed in the uppermost mantle (V_{Pn}), arrival time estimates for *SsPmp* depend on a trade-off between V_{Pn} and *H*. To remove uncertainties due

to the trade-off between V_{Pn} and H, this study used an assumed V_{Pn} value reported in Pei et al. (2007) for waveform fitting. The *Pn*-wave velocity shows only minor variation (7.9–8.1 km/s) along our profile (Fig. S1).

From east to west, the estimated crustal thicknesses (H_{VDSS}) along the profile (Fig. 3c) increases smoothly from 43 km beneath the outer zone (at a projected distance of 850 km) to 51 km beneath the intermediate zone (at a projected distance of 550 km). H_{VDSS} increases from ~54 km at a projected distance of 500 km to a maximum value of ~68 km beneath the inner zone (at a projected distance of 350 km). The Moho then shallows gradually westward to 50 km beneath the Red-River fault (at a projected distance of 50 km). An unusually thickened crust occurs beneath the eastern part of the inner zone, between the Lvzhijiang-Yuanmou and Xiaojiang faults. Fig. S2 shows the cross section of receiver functions using the same earthquake.

4. Discussion

4.1. The high-velocity lower crustal roots of the ELIP

P-wave receiver functions can also image crustal structure (Yuan et al., 1997). For comparison, Fig. 5b shows receiver functions migrated with a similar back-azimuth as that used for VDSS data. The strong red amplitude band in Fig. 5b indicates the Moho (Chen et al., 2015). The receiver function method provided maximum crustal thickness estimates of ~60 km or about 8 km less than results from the VDSS method (the black dashed line). The crustal thickness estimate from DSS analysis (Xu et al., 2015) was even less than the result obtained from receiver function analysis (Chen et al., 2015) of the same profile (Fig. 5b). As suggested in Fig. 2, disparate results from different seismic methods may arise due to complex crustal velocity structure. DSS methods use active-source seismic sounding to detect the fine-scale crustal structure with high frequency seismic waves. DSS results are therefore less sensitive to deeper discontinuity surfaces. Receiver function methods use *Pms* phases to detect subsurface structure, but these are subject to interference from strong discontinuities near the Moho in cases of a multi-layered crust to upper-mantle transition. VDSS methods estimate crustal thickness from the *SsPmp* phase, which is a conversion of a teleseismic *S*-wave totally reflected by the Moho. The ray-parameters for the direct *Ss* phase from the two earthquakes (Table 1) of 0.1330–0.1341 s/km and 0.1353–0.1362 s/km (respectively) constrain the maximum lower crustal *P*-wave velocity at ~7.4 km/s. The difference between DSS and VDSS results reveals a high-velocity lower crustal body (HVLCB) beneath the inner zone. Crustal thickness estimates from DSS analysis actually record an upper discontinuity belonging to the HVLCB whereas the VDSS results record the lower
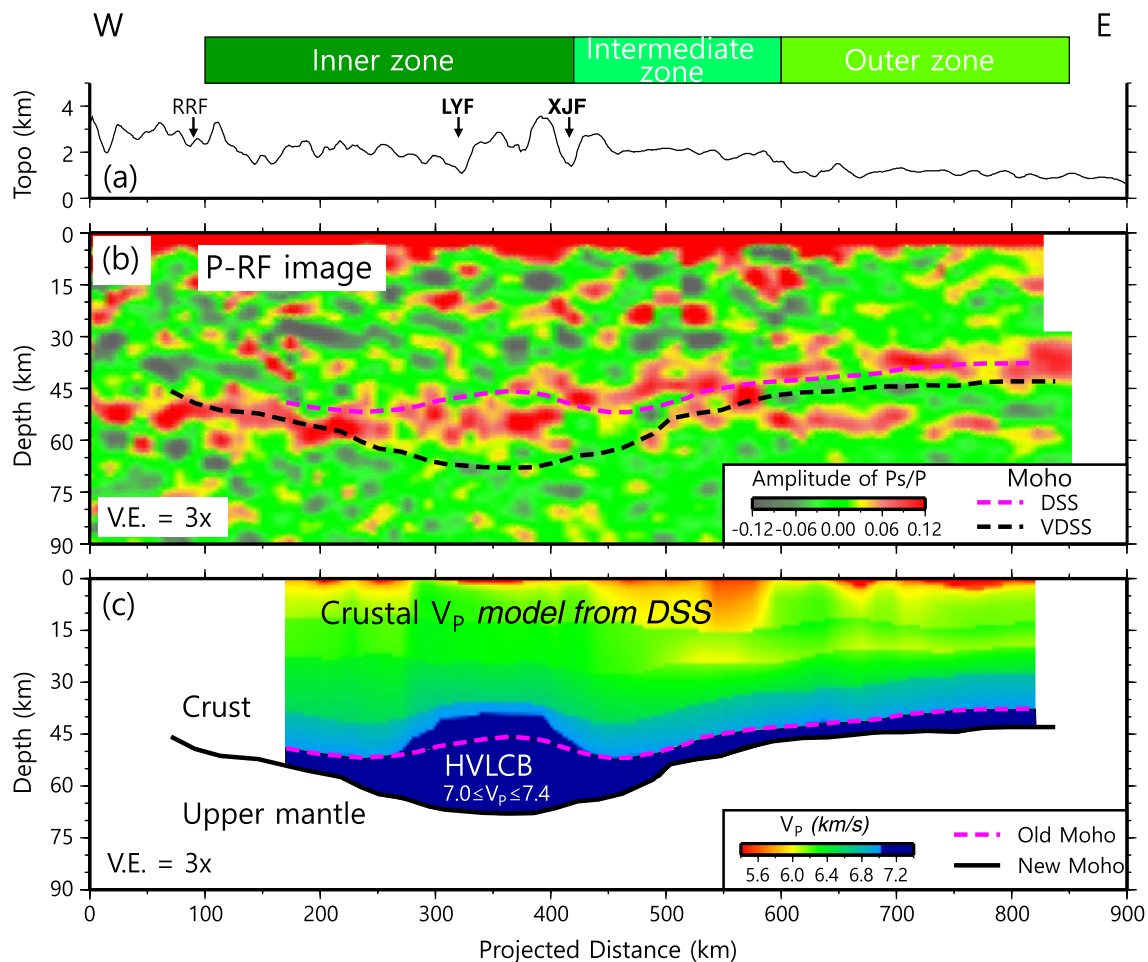

Fig. 5. (a) Topography of the east-west trending profile across the ELIP. The main faults covered by the profile (F1, F2 and F3 in Fig. 1) are identified by their respective abbreviations with locations marked by small arrows (RRF, Red River Fault; LYF, Lvzhijiang-Yuanmou Fault; XJF, Xiaojiang Fault). (b) Migrated image of the crustal structure based on common conversion point technique applied to the stacked receiver function (Chen et al., 2015). Only receiver functions with similar back-azimuth were used as VDSS data for imaging. The pink dashed line indicates the Moho topography obtained from wide-angle seismic reflection/refraction data (Xu et al., 2015), while the black dashed line is from this study. (c) Crustal *P*-wave velocity structure obtained from DSS (Xu et al., 2015). The pink dashed line depicts the DSS-based Moho, while the black continuous line indicates the VDSS-based Moho. A high velocity lower crustal body (HVLCB), with *P*-wave velocity between 7.0 and 7.4 km/s, appears as two crust-mantle boundaries derived from two different methods. Vertical exaggeration in (b) and (c) is 3:1. (For interpretation of the references to color in this figure legend, the reader is referred to the web version of this article.)

discontinuity of the HVLCB. The *Pms* phase within the receiver functions is thus contaminated by the HVLCB velocity gradient. Other LIPs with relatively high *P*-wave velocities of 7.0–7.6 km/s exhibit the same type of feature, including the Ontong Java and Kerguelen-Broken Ridge oceanic plateaus, North Atlantic volcanic passive margins, Deccan Traps, and Columbia River Basalt Group (Coffin and Eldholm, 1994).

4.2. High density of the HVLCB derived from airy isostasy

According to Airy-type crustal isostasy, the crustal thickness *H* can be estimated by

$$H = \frac{\rho_m}{\rho_m - \rho_c} h + H_0$$

where ρ_c is the crustal density (~ 2.75 g/cm^3), ρ_m is the upper mantle density (~ 3.20 g/cm^3), h is the topographic elevation (Fig. 3a), and H_0 is the reference crustal thickness (global average value of 33 km).

The crustal thickness predicted by the Airy model reaches depths of 50–55 km beneath the inner zone and 43 km beneath the outer zone (Fig. 3c). The results are consistent with the seismically determined crustal thickness in the outer zone but give thinner estimates for the inner zone (Fig. 3c and d). Gravity inversion of the COMGRA-ELIP experiment reveals a high density anomaly of ~ 3.14 g/cm^3 in the lower crust beneath the inner zone at depths of ~ 41 km (Deng et al., 2014b; Deng et al., 2016). This anomaly could give lower crustal thickness estimates in Airy models than those generated by our methods for the inner zone. Given the correspondence between the 3.14 g/cm^3 density and *P*-wave velocity of ~ 7.2 km/s, the high-density lower crust also indicates the presence of a HVLCB (Birch, 1960, 1961).

The VDSS method assumes a uniform average crustal velocity model. If the HVLCB exists, the crustal average V_P will increase 0.1 km/s and cause variation of about ± 4 km in estimating crustal thickness. Gravity inversion analysis treated the Moho as flat and detected a high-density lower crustal body in the inner zone (Deng et al., 2016). A positive density anomaly causes the Moho to rest deeper at the isostatic equilibrium, however, because the high-density lower crust increases the total mass of inner zone and thus requires more buoyancy. We interpret this crustal body between the discontinuities obtained from the DSS and VDSS as the HVLCB. The thickness of the HVLCB is about 15–20 km (Fig. 5c). Using crust and mantle density values from Deng et al. (2016) as inputs, we estimated the density of the HVLCB by isostasy. The density of the HVLCB is only ~ 0.03 g/cm^3 greater than estimates for lower crustal density by gravity inversion (Deng et al., 2016).

4.3. Mechanism for HVLCB formation

When integrated with the velocity structure from the DSS (Xu et al., 2015), receiver function analysis (Chen et al., 2015), and other studies (Coffin and Eldholm, 1994; Liu et al., 2001), the results reported here indicate a high-V_P velocity lower crustal body (7.0–7.4 km/s) in the inner zone of the ELIP (Fig. 5c). The *P*-wave velocity in the lower crustal body is significantly higher than that of normal continental or oceanic crust (Catchings and Mooney, 1988). The HVLCB is inferred to be genetically related to the ELIP for the following reasons. First, the thickness of the HVLCB gradually decreases from the inner zone (~ 68 km) to the intermediate zone (~ 54 km). This spatial pattern matches that which would be expected from mantle plume emplacement (Xu et al., 2004), wherein the inner zone experiences more extensive melting than the intermediate and outer zones. Second, the distribution of the HVLCB matches the spatial pattern of the crustal dome suggesting that the HVLCB likely formed from an ancient mantle plume (Xu and He, 2007; Deng et al., 2014a, 2014b). As discussed by He et al. (2003), formation of the dome immediately preceding eruption of the basalts most likely resulted from thermal or structural doming by the mantle plume that generated the Emeishan basalts.

Receiver function and residual gravity analysis detected a high-density, high-V_P and high-V_P/V_S lower crust at this locality (Chen et al., 2015; Deng et al., 2016). The mantle plume uplifted the lithosphere and caused ELIP emplacement in the late Permian along with intrusive magmatism. This led to crustal accretion at the bottom of the crust and flood basalt accumulation around the inner, topographically elevated region. Accreted magmas and associated fractionated materials cooled and formed a high-density HVLCB beneath the original crust (Chen et al., 2015; Deng et al., 2016). As a consequence, a new Moho formed at the bottom of the HVLCB. The thermal gradient across the domal structure creates a zonal variation in crustal structure (Xu et al., 2004).

4.4. Volume of Emeishan magmas

The late Permian ELIP includes only around 0.25 million km^2 of basalt exposed at the surface (He et al., 2003). The thickness of the HVLCB estimated by seismic tomography is 15–25 km (Liu et al., 2001). The high-density lower crust is imaged at ~ 40 km depth with a thickness of ~ 20 km according to receiver function analysis (Deng et al., 2014a; Chen et al., 2015; Deng et al., 2016). Our results indicate a lower crustal thickness of ~ 17 km between the initial Moho acquired from DSS (Xu et al., 2015) and the newly detected Moho from VDSS. The thickness of the ELIP HVLCB therefore resembles that observed in association with the Ontong Java LIP (~ 16 km) (Furumoto et al., 1976). Assuming the inner zone includes this layer gives an estimate of 1.6×10^6 km^3 for the ELIP HVLCB. The maximum and minimum intrusive/extrusive ratios (White et al., 2006) give a total volume estimate of 1.76–3.2×10^6 km^3 for the ELIP. These new estimates approach volumes estimated for typical continental flood basalts, such as the Deccan Traps (Verma and Banerjee, 1992; Coffin and Eldholm, 1994) and the Columbia River Basalt Group (Coffin and Eldholm, 1994).

5. Conclusions

VDSS results detected strong total reflections returning from a depth of ~ 60–70 km and indicating an unusually thickened crust with a maximum V_P of ~ 7.4 km/s beneath the inner zone of the ELIP. Together with a prominent interface observed at depths of 50 km in receiver function images, deep seismic sounding revealed a ~ 17 km thick HVLCB at the base of the crust beneath the area bounded by the Lvzhijiang-Yuanmou Fault to the west and by the Xiaojiang Fault to the east. Gravity inversion of the COMGRA-ELIP also detected a high density anomaly indicative of a HVLCB beneath the ELIP. Magmatic ponding and fractionation during Emeishan plume activity caused crustal thickening and shifted the crust-mantle boundary to the bottom of HVLCB (new Moho). The refined crustal structure allows new estimates for the volume of Emeishan magmas of 1.76–3.2×10^6 km^3. This volume falls within a range typical of plume-generated LIPs around the world.

Supplementary data to this article can be found online at https://doi.org/10.1016/j.tecto.2017.10.009.

References

Birch, F., 1960. The velocity of compressional waves in rocks to 10 kilobars, part 1. J. Geophys. Res. 65, 1083–1102.

Birch, F., 1961. The velocity of compressional waves in rocks to 10 kilobars, part 2. J. Geophys. Res. 66, 2199–2224.

Catchings, R.D., Mooney, W.D., 1988. Crustal structure of the Columbia Plateau - evidence for continental rifting. J. Geophys. Res. Solid Earth 93, 459–474.

Chen, Y.L., Niu, F.L., Liu, R.F., Huang, Z.B., Tkalcic, H., Sun, L., Chan, W., 2010. Crustal structure beneath China from receiver function analysis. J. Geophys. Res. Solid Earth 115, 22.

Chen, Y., Xu, Y.G., Xu, T., Si, S.K., Liang, X.F., Tian, X.B., Deng, Y.F., Chen, L., Wang, P., Xu, Y.H., Lan, H.Q., Xiao, F.H., Li, W., Zhang, X., Yuan, X.H., Badal, J., Teng, J.W., 2015. Magmatic underplating and crustal growth in the Emeishan Large Igneous Province, SW China, revealed by a passive seismic experiment. Earth Planet. Sci. Lett. 432, 103–114.

Coffin, M.F., Eldholm, O., 1994. Large igneous provinces - crustal structure, dimensions, and external consequences. Rev. Geophys. 32, 1–36.

Coffin, M.F., Eldholm, O., 2001. Large igneous provinces: progenitors of some ophiolites? In: Mantle Plumes: Their Identification Through Time, pp. 59–70.

Cui, Z.Z., Lu, D.Y., Chen, J.P., Zhang, Z.Y., Huang, L.Y., 1987. The deep structural and tectonic features of the crust in Panxi area. Acta Geophys. Sin. 30, 566–580.

Deng, Y.F., Zhang, Z.J., Mooney, W., Badal, J., Fan, W.M., Zhong, Q., 2014a. Mantle origin of the Emeishan large igneous province (South China) from the analysis of residual gravity anomalies. Lithos 204, 4–13.

Deng, Y.F., Zhang, Z.J., Fan, W.M., Perez-Gussinye, M., 2014b. Multitaper spectral method to estimate the elastic thickness of South China: implications for intracontinental deformation. Geosci. Front. 5, 193–203.

Deng, Y.F., Chen, Y., Wang, P., Essa, K.S., Xu, T., Liang, X.F., Badal, J., 2016. Magmatic underplating beneath the Emeishan large igneous province (South China) revealed by the COMGRA-ELIP experiment. Tectonophysics 672, 16–23.

Dobretsov, N.L., Kirdyashkin, A.A., Kirdyashkin, A.G., Vernikovsky, V.A., Gladkov, I.N., 2008. Modelling of thermochemical plumes and implications for the origin of the Siberian traps. Lithos 100, 66–92.

Farnetani, C.G., Richards, M.A., Ghiorso, M.S., 1996. Petrological models of magma evolution and deep crustal structure beneath hotspots and flood basalt provinces. Earth Planet. Sci. Lett. 143, 81–94.

Furlong, K.P., Fountain, D.M., 1986. Continental crustal underplating: thermal considerations and seismic-petrologic consequences. J. Geophys. Res. 91 (B8), 8285–8294.

Furumoto, A.S., Webb, J.P., Odegard, M.E., Hussong, D.M., 1976. Seismic studies on Ontong Java Plateau, 1970. Tectonophysics 34, 71–90.

He, B., Xu, Y.G., Chung, S.L., Xiao, L., Wang, Y., 2003. Sedimentary evidence for a rapid, kilometer-scale crustal doming prior to the eruption of the Emeishan flood basalts. Earth Planet. Sci. Lett. 213, 391–405.

King, S.D., Anderson, D.L., 1998. Edge-driven convection. Earth Planet. Sci. Lett. 160, 289–296.

Larson, R.L., 1991. Latest pulse of earth - evidence for a Midcretaceous Superplume. Geology 19, 547–550.

Li, S.L., Mooney, W.D., Fan, J.C., 2006. Crustal structure of mainland China from deep seismic sounding data. Tectonophysics 420, 239–252.

Liu, J.H., Liu, F.T., He, J.K., Chen, H., You, Q.Y., 2001. Study of seismic tomography in Panxi paleorift area of southwestern China - structural features of crust and mantle and their evolution. Sci. China Ser. D Earth Sci. 44, 277–288.

Morgan, W.J., 1971. Convection plumes in lower mantle. Nature 230, 42–43.

Pei, S.P., Zhao, J.M., Sun, Y.S., Xu, Z.H., Wang, S.Y., Liu, H.B., Rowe, C.A., Toksoz, M.N., Gao, X., 2007. Upper mantle seismic velocities and anisotropy in China determined through Pn and Sn tomography. J. Geophys. Res. Solid Earth 112, 16.

Randall, G.E., 1989. Efficient calculation of differential seismograms for lithospheric receiver functions. Geophys. J. Int. 99, 469–481.

Rogers, G.C., 1982. Oceanic plateaus as meteorite impact signatures. Nature 299, 341–342.

Sun, Y., Niu, F.L., Liu, H.F., Chen, Y.L., Liu, J.X., 2012. Crustal structure and deformation of the SE Tibetan plateau revealed by receiver function data. Earth Planet. Sci. Lett. 349, 186–197.

Tian, X.B., Chen, Y., Tseng, T.L., Klemperer, S.L., Thybo, H., Liu, Z., Xu, T., Liang, X.F., Bai, Z.M., Zhang, X., Si, S.K., Sun, C.Q., Lan, H.Q., Wang, E.C., Teng, J.W., 2015. Weakly coupled lithospheric extension in southern Tibet. Earth Planet. Sci. Lett. 430, 171–177.

Tseng, T.L., Chen, W.P., Nowack, R.L., 2009. Northward thinning of Tibetan crust revealed by virtual seismic profiles. Geophys. Res. Lett. 36, 5.

Verma, R.K., Banerjee, P., 1992. Nature of continental-crust along the Narmada-Son lineament inferred from gravity and deep seismic-sounding data. Tectonophysics 202, 375–397.

Wessel, P., Smith, W.H.F., 1998. New, improved version of generic mapping tools released. EOS Trans. Am. Geophys. Union 79, 1.

White, R., Mckenzie, D., 1989. Magmatism at rift zones - the generation of volcanic continental margins and flood basalts. J. Geophys. Res. Solid Earth 94, 7685–7729.

White, S.M., Crisp, J.A., Spera, F.J., 2006. Long-term volumetric eruption rates and magma budgets. Geochem. Geophys. Geosyst. 7.

Xiong, S.B., Zheng, Y., Yin, Z.X., Zeng, X.X., Quan, Y.L., Sun, K.Z., 1993. The 2-D structure and it's tectonic implications of the crust in the Lijiang-Panzhihua-Zhehai region. Acta Geophys. Sin. 36, 434–444.

Xu, Y.G., He, B., 2007. Thick, high-velocity crust in the Emeishan large igneous province, SW China: evidence for crustal growth by magmatic underplating or intraplating. Geol. Soc. Am. 430, 841–858.

Xu, Y.G., He, B., Chung, S.L., Menzies, M.A., Frey, F.A., 2004. Geologic, geochemical, and geophysical consequences of plume involvement in the Emeishan flood-basalt province. Geology 32, 917–920.

Xu, T., Zhang, Z.J., Liu, B.F., Chen, Y., Zhang, M.H., Tian, X.B., Xu, Y.G., Teng, J.W., 2015. Crustal velocity structure in the Emeishan large igneous province and evidence of the Permian mantle plume activity. Sci. China Earth Sci. 58, 1133–1147.

Yu, C.Q., Chen, W.P., van der Hilst, R.D., 2013. Removing source-side scattering for virtual deep seismic sounding (VDSS). Geophys. J. Int. 195, 1932–1941.

Yuan, X.H., Ni, J., Kind, R., Mechie, J., Sandvol, E., 1997. Lithospheric and upper mantle structure of southern Tibet from a seismological passive source experiment. J. Geophys. Res. Solid Earth 102, 27491–27500.

Zhang, Y.X., Luo, Y., Yang, X., 1988. The Panxi Rift. Geological Press, Beijing.